Electronic structure of the quantum spin Hall parent compound CdTe and related topological issues

Jie Ren,[1,2,3] Guang Bian,[4] Li Fu,[1,*] Chang Liu,[4] Tao Wang,[1] Gangqiang Zha,[1] Wanqi Jie,[1] Madhab Neupane,[4] T. Miller,[2,3] M. Z. Hasan,[4] and T.-C. Chiang[2,3,5,†]

[1]*State Key Laboratory of Solidification Processing, School of Materials Science and Engineering, Northwestern Polytechnical University, Xi'an 710072, China*

[2]*Department of Physics, University of Illinois at Urbana-Champaign, 1110 West Green Street, Urbana, Illinois 61801-3080, USA*

[3]*Frederick Seitz Materials Research Laboratory, University of Illinois at Urbana-Champaign, 104 South Goodwin Avenue, Urbana, Illinois 61801-2902, USA*

[4]*Joseph Henry Laboratory and Department of Physics, Princeton University, Princeton, New Jersey 08544, USA*

[5]*Synchrotron Radiation Center, University of Wisconsin-Madison, 3731 Schneider Drive, Stoughton, Wisconsin 53589, USA*

(Received 25 July 2014; published 17 November 2014)

Cadmium telluride (CdTe), a compound widely used in devices, is a key base material for the experimental realization of the quantum spin Hall phase. We report herein a study of the electronic structure of CdTe by angle-resolved photoemission spectroscopy from well-ordered (110) surfaces. The results are compared with first-principles calculations to illustrate the topological distinction between CdTe and a closely related compound HgTe. Through a theoretical simulation a topological phase transition as well as the Dirac-Kane semimetal phase at the critical point was demonstrated in the mixed compound $Hg_xCd_{1-x}Te$.

DOI: 10.1103/PhysRevB.90.205211 PACS number(s): 71.20.Nr, 71.70.Ej, 71.18.+y

I. INTRODUCTION

Cadmium telluride (CdTe) is a semiconductor with a direct band gap of 1.44 eV. Ever since the 1960s CdTe has been widely used for electro-optic modulators and nonlinear optics in both the near and far infrared regions, transferred electron devices based on the Gunn effect, piezoelectric devices, electroluminescent diodes, infrared windows, solar cells, and detectors for α, β, x, and γ radiations [1–9]. The properties making CdTe so versatile are high atomic numbers, a large band gap, a high electron mobility of $\sim$1100 cm^2/Vs, and the greatest electro-optic coefficient among the II-VI compound crystals [10–14]. In recent years, CdTe has been employed as a key parent material for the experimental realization of the quantum spin Hall phase that forms the basis for two-dimensional (2D) topological insulators [15–18]. The HgTe/CdTe quantum well systems, with the two components belonging to different three-dimensional (3D) time reversal Z_2 topological phases, possess protected spin-polarized edge states because of an "inverted" band alignment across the boundary [15,16]. By tuning the chemical composition of the mixed compound $Hg_xCd_{1-x}Te$ to a proper critical value, a 3D massless Dirac-Kane fermion can be realized [19–23]. The conical dispersion in all three dimensions makes this compound scientifically interesting and highly promising for next generation electronic device applications.

With much improved crystal growth techniques, high-quality CdTe single crystals have become available with a high resistivity and in large dimensions (centimeters) suitable for large-scale integrated device fabrication. The electronic structure of CdTe has been studied by various theoretical and experimental methods [24–28]. However, high-resolution band mapping has been lacking to this date. The detailed low-energy electronic structure of CdTe is thus unavailable, but it is of fundamental importance for understanding the topological properties and trends of this type of material. To address this issue, we have performed high-resolution angle-resolved photoemission spectroscopy (ARPES) measurements of samples prepared by cleavage *in situ* to expose clean, well-ordered, and flat surfaces. These surfaces exhibited much sharper spectral features than samples prepared by sputtering and annealing, thus facilitating precise placement of the band edges. The results from 3D band mapping, compared with first-principles calculations, allow us to identify the orbital characters and spin-split gaps of the valence bands close to the Fermi level. The results are compared with those of HgTe to demonstrate the critical differences in their band structures that related to the formation of the quantum spin hall phase. The topological phase transition from CdTe to HgTe upon alloying and the massless Dirac-Kane semimetal phase at the critical composition are illustrated by computations based on a mixed-pseudopotential simulation. The experiment and theory together offer a comprehensive understanding on the electronic behavior of CdTe and related topological issues.

II. METHODS

In our work, electronic band structures were computed from first principles using a plane-wave basis set and the pseudopotentials developed by Hartwigsen, Goedecker, and Hutter [29]. The main computation package based on local density approximation including spin-orbit coupling (SOC) was developed by the ABINIT group [30,31]. Large single crystals of CdTe were grown by a modified Bridgman method [32]. Samples used in the experiment were cleaved *in situ* under ultrahigh vacuum ($< 10^{-10}$ Torr) prior to ARPES measurements at the Synchrotron Radiation Center of the University of Wisconsin-Madison using 24 eV photons and the Scienta R4000 endstation on the Plane-Grating-Monochromator Beamline.

*Corresponding author: fuli@nwpu.edu.cn
†Corresponding author: tcchiang@illinois.edu

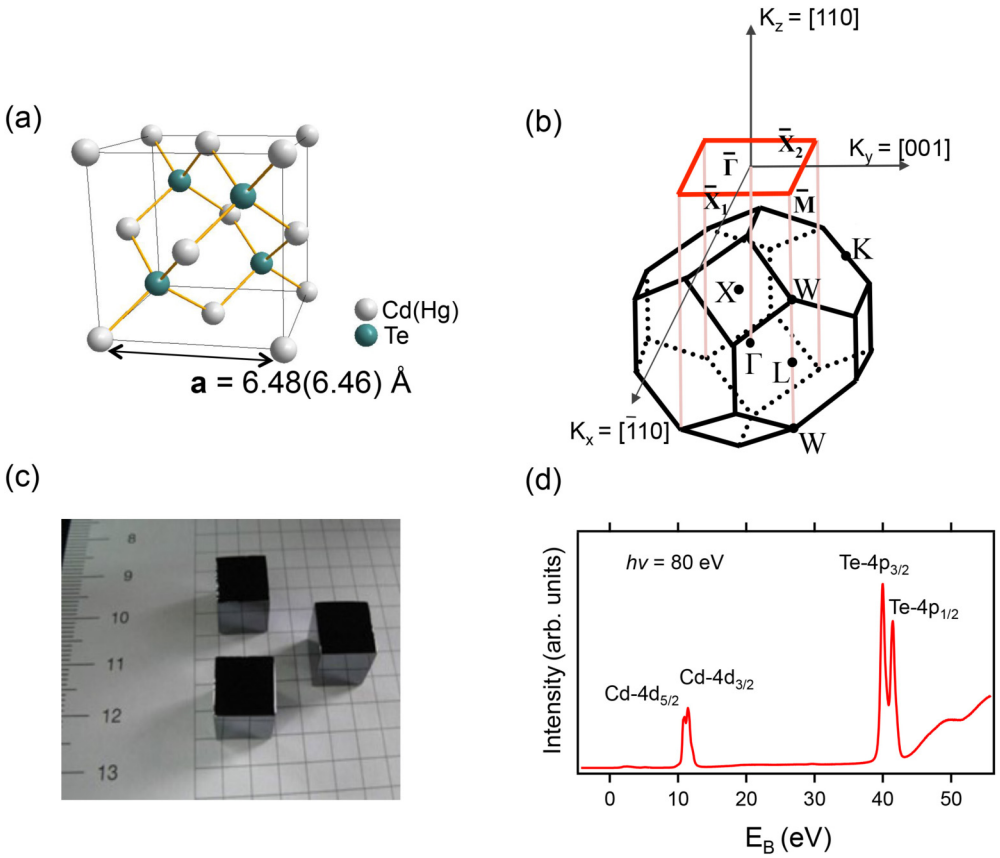

FIG. 1. (Color online) (a) Zincblende lattice structure of Cd(Hg)Te. (b) Bulk Brillouin zone and (110) surface Brillouin zone with high symmetry points indicated. (c) Photograph of CdTe single crystals samples. (d) Photoemission from core levels of CdTe measured with 80 eV photons.

III. RESULTS AND DISCUSSION

Crystals of CdTe adopt the zincblende structure with a cubic lattice constant of $a = 6.48$ Å at room temperature. The structure is the same as that of diamond, but with Cd and Te atoms occupying two different sites in the unit cell [Fig. 1(a)]. Each Cd (Te) is surrounded by four Te (Cd) atoms to form a tetrahedral bonding configuration. The structure, without spatial inversion symmetry, is noncentrosymmetric. The natural cleavage plane is (110). The Brillouin zone is shown in Fig. 1(b). The k_x, k_y, and k_z axes are chosen to be along [1-10], [001], and [110], respectively. The W and L points are projected onto the $\bar{M}$ points of the (110) surface Brillouin zone, which is indicated by the red rectangle with size $(\sqrt{2},1)\pi/a$ as shown in Fig. 1(b). A photograph of the CdTe crystals used in the experiment is shown in Fig. 1(c). The resistivity of the samples is 6×10^9 Ωcm at room temperature. An overview ARPES spectrum taken with a photon energy of 80 eV [Fig. 1(d)] reveals two pairs of sharp peaks. They correspond to the Cd $4d$ and Te $4p$ core levels at binding energy $E_B \approx 11$ and 40 eV, respectively. The valence bands near the Fermi level, much weaker relative to the core levels, are not apparent in this spectrum.

Figures 2(a) and 2(b) show the calculated band structures of CdTe with and without SOC. The electronic and optical properties of this material are mainly determined by three sets of bands close to the Fermi levels. These are labeled as Γ_6, Γ_7, and Γ_8 in terms of the representations of the point group at Γ. Band Γ_6 is primarily derived from the Cd $5s$ orbitals while Γ_7 and Γ_8 originate from the Te $5p$ orbitals. These atomic orbital characters are evident from the calculated charge density distribution of each state as illustrated in Fig. 2(e). States Γ_6, Γ_7, and Γ_8 are two-, two-, and fourfold degenerate at Γ, respectively, and they split into multiple bands as they disperse away from Γ due to reduced symmetry. Specifically, the Γ_8 band splits into a heavy-hole band and a light-hole band. As shown in Fig. 2(a), the electronlike Γ_6 band is located above the Fermi level while the holelike Γ_7 and Γ_8 bands are below the Fermi level. The energy gap between the Γ_6 and Γ_8 states is 0.78 eV, which is smaller than the experimental value of 1.44 eV. This roughly a factor of 2 discrepancy is quite common for local density calculations, which produce very accurate valence band dispersions but tend to underestimate energy gaps in semiconductors and insulators. With the SOC turned off in the calculation, the spin-split Γ_7 and Γ_8 bands become degenerate at Γ.

Similarly calculated results for HgTe are presented in Figs. 2(c) and 2(d) for comparison. A key difference between HgTe and CdTe is the band ordering at the zone center. For HgTe, the Γ_8 states are located above the Γ_6 states. Therefore, the energy difference $\Delta E = E_{\Gamma 6} - E_{\Gamma 8}$ is positive for CdTe but negative for HgTe. This change in sign signifies that CdTe and HgTe belong to different topological phases. As established in previous studies, HgTe is topologically

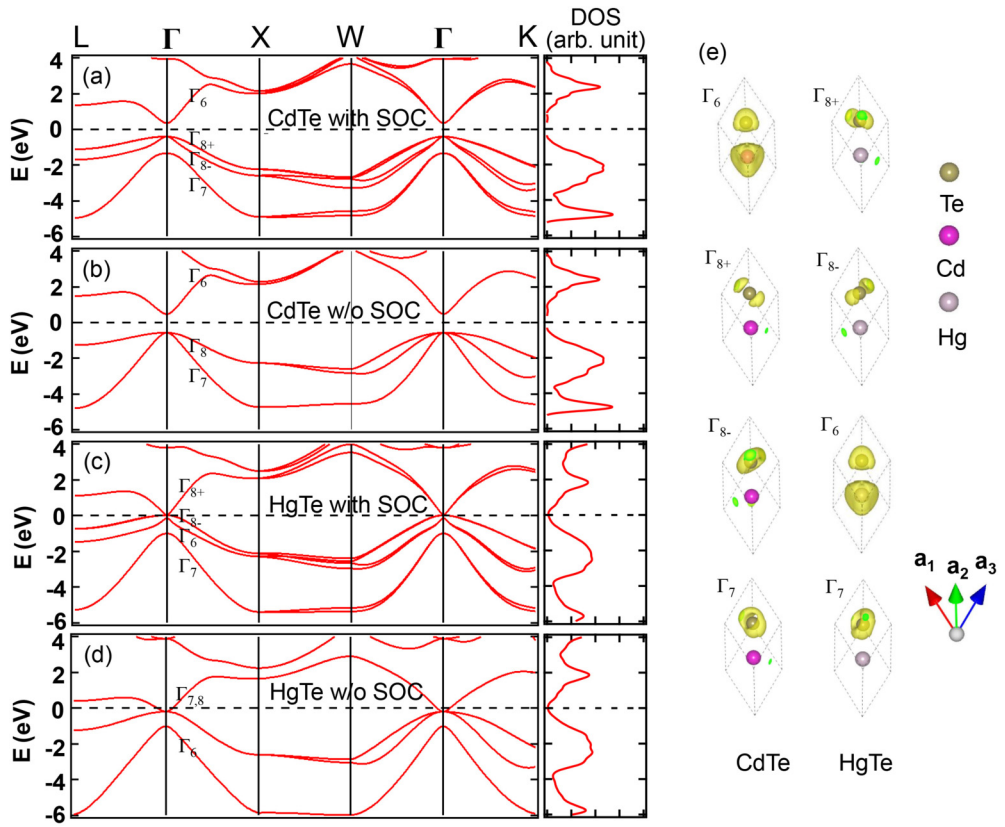

FIG. 2. (Color online) Calculated band structure and density of states (DOS) of (a) CdTe with SOC, (b) CdTe without SOC, (c) HgTe with SOC, and (d) HgTe without SOC. (e) Charge density distributions of states at the Γ point. The arrows indicate the orientation of the unit cell.

nontrivial and supports topological surface states within the energy gap between the "inverted" Γ_6 and Γ_8 bands [33,34]. Rigorously speaking, HgTe is a semimetal, not an insulator, but its topological order can still be defined in the same way as for other topological insulators. The calculated density of states (DOS) is plotted in Fig. 2. The curves (with energy smearing 0.005 hartree) reflect the semiconducting and semimetallic natures for CdTe and HgTe, respectively.

Figure 3(a) presents the calculated projected bulk bands of CdTe along the k_x direction of the (110) plane. Each band corresponds to a k_z of a dense grid. The bulk bands with $k_z = 0$ are shown in red, which correspond to the edges (or extremes) of the bulk band continua. ARPES taken with a photon energy (24 eV) away from direct transitions should yield an intensity map resembling the projected density of states, and the results are shown in Figs. 3(b) and 3(c). The Fermi level is located at 0.3 eV above the valence band maximum, which is consistent with the high resistivity of our sample at room temperature. The heavy-hole (HH, Γ_{8+}), light-hole (LH, Γ_{8-}), and split-off (SO, Γ_7) bands are resolved in the data as edges of emission from the projected bulk bands. Specifically, the emission intensity pattern is proportional to the one-dimensional (1D) density of states $(E_C - E)^{-1/2}\Theta(E_C - E)$ near each band edge at $E_C(k_{x,y})$ [35]. This leads to a strong buildup of emission intensity as the energy approaches the band edge from below and a cutoff (rounded by lifetime effects) at the band edge.

At the zone center the Γ_7 state is at 0.92 eV below the Γ_8 states based on both experiment and theory, which is an indication of the SOC strength. From curve fitting, the experimentally determined effective masses are $m^*_{\rm HH} = 0.8m_0$, $m^*_{\rm LH} = 0.12m_0$, and $m^*_{\rm SO} = 0.19m_0$, where m_0 is the free electron mass. These spectroscopic effective masses are in good accord with results obtained from prior cyclotron resonance measurements [36]. Such ARPES measurements were performed for a dense set of in-plane emission directions of $\mathbf{k}_\parallel$ to yield a 3D data set. A stack of ARPES constant-energy maps is shown in Fig. 3(d); evidently, the dispersive shape of each valence band evolves in a similar way. At the top of the band, the contour is a point at Γ. Moving below the band top, it develops into an elliptical shape first and then further develops into a distorted/warped rectangle. The details are revealed in Fig. 3(e) with the data symmetrized to avoid cross section variations. The elliptical and warped rectangular shapes of the energy band contours are consistent with the symmetry of the (110) surface where the x and y directions are inequivalent.

To highlight the distinction between the band structures of CdTe and HgTe, ARPES spectra taken from the (110) surfaces of both materials and first-principles band structures are presented in Figs. 4(a)–4(d). The Fermi level in HgTe is at the top of the valence bands, resulting in a pointlike Fermi surface and a semimetallic behavior. At first glance, the ARPES data for HgTe seems quite similar to that of CdTe but with a shifted Fermi level. However, prior spin-resolved measurements have shown that the inner band marked by the red arrow in Fig. 4(b) is actually a topological surface state (TSS) band connecting from the Γ_6 band to the upper Γ_8 band (above the Fermi level) as illustrated in Fig. 4(d) [34].

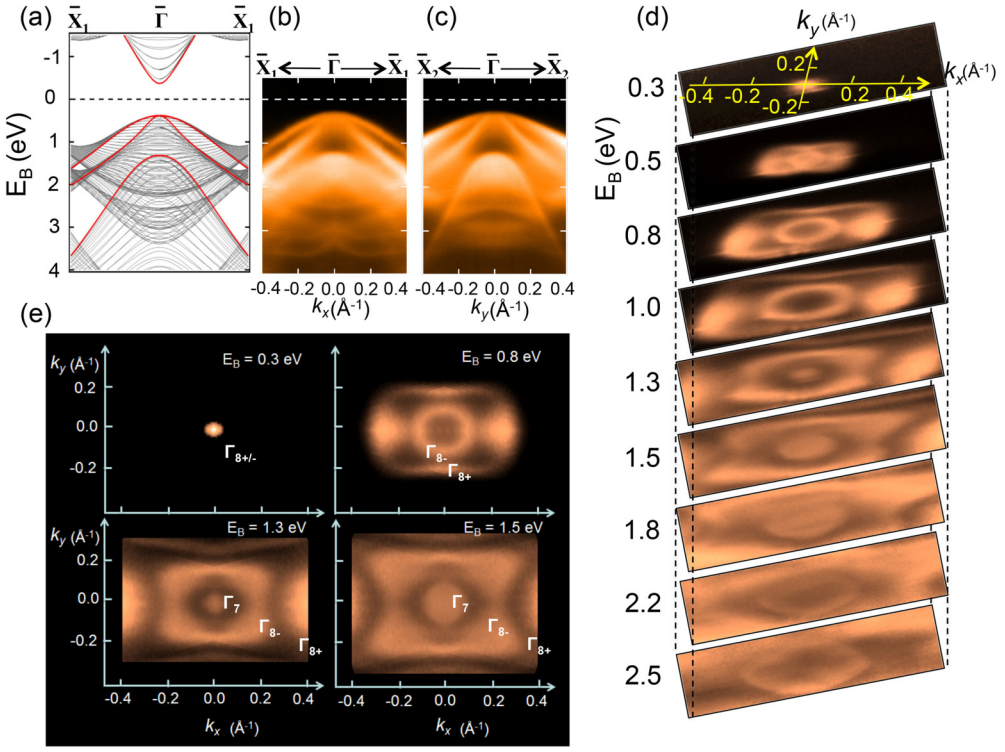

FIG. 3. (Color online) (a) Calculated projected bulk bands of CdTe along $\bar{\Gamma}\bar{X}_1$ in the (110) surface Brillouin zone. Bulk bands with $k_z = 0$ are shown as red curves. (b) APRES spectrum taken along $\bar{\Gamma}\bar{X}_1$. (c) ARPES spectrum taken along $\bar{\Gamma}\bar{X}_2$. (d) Stack of ARPES isoenergy maps in the k_x-k_y plane. (e) Symmetrized isoenergy maps at four different binding energies.

Note that this TSS band has a needlelike shape with its apex higher than the calculated bulk Γ_6 band maximum. Furthermore, this band is very narrow in the ARPES data, distinctly different from the band-edge features that are broader and resemble 1D density of states. The difference is particularly striking when the results are compared with those for CdTe. Whenever a surface state band appears near a bulk band edge, the oscillator strength is transferred from the

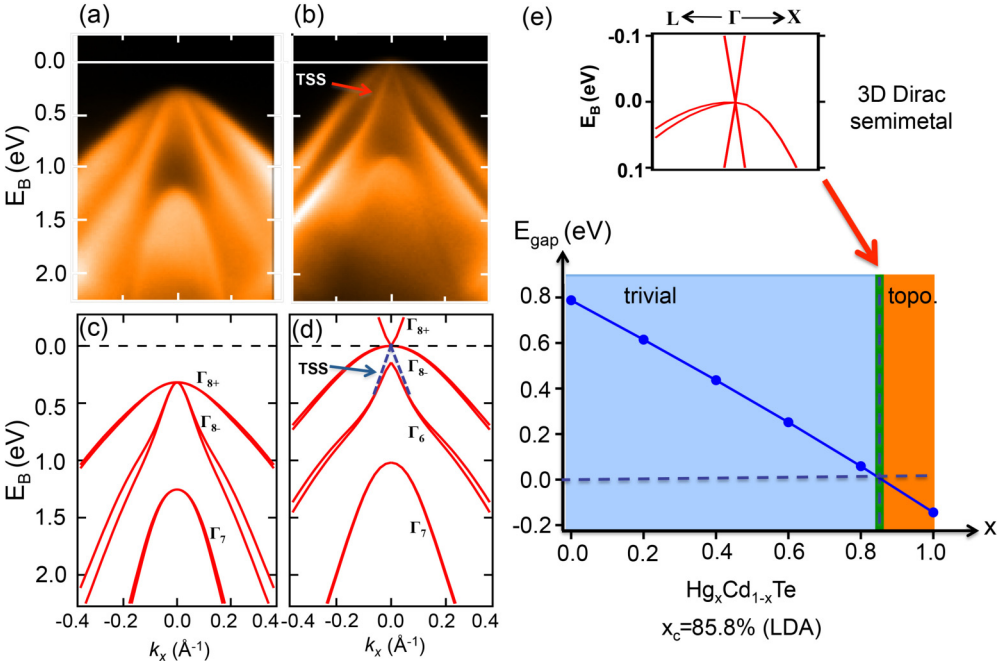

FIG. 4. (Color online) Experimental ARPES maps along k_x for (a) CdTe and (b) HgTe. The corresponding calculated bands of (c) CdTe and (d) HgTe. (e) The phase diagram of $Hg_xCd_{1-x}Te$. The upper panel shows the band structure of $Hg_xCd_{1-x}Te$ at the critical composition $x_c = 85.8\%$.

bulk band states to the surface band, resulting in suppressed bulk emission as is apparently the case here for HgTe [37]. This comparison provides a strong indication for the different electronic structure between CdTe and HgTe.

The inverted ordering of the Γ_6 and Γ_8 bands in HgTe results in an opposite "adiabatic parity" scenario [17,33] and makes the case topologically distinctive from CdTe. By varying the chemical composition in $Hg_xCd_{1-x}Te$ it is possible to transform from one case to the other through a topological phase transition. At the critical composition x_c, the band gap vanishes, and the system becomes a 3D Dirac-Kane semimetal. Figure 4(e) presents the calculated bulk energy gap as a function of Hg concentration x based on a mixed pseudopotential method [38]. The theoretical critical concentration is $x_c = 0.858$, which is very close to a previous experimentally suggested value 0.83 [19]. The band structure of the Dirac-Kane semimetal, presented in the upper panel of Fig. 4(e), shows the "touching" of Γ_6 and Γ_8 bands, and the resulting linear bulk band dispersion. Generally, such 3D Dirac-like band dispersion can potentially split into a pair of Weyl fermions if the space inversion symmetry is broken [21,39]. The resulting Weyl semimetal phase has a nonzero topological Chern number and hosts exotic spin-filtered Fermi arc surface states [21,39]. While $Hg_xCd_{1-x}Te$ at x_c lacks inversion symmetry, it does not show such Weyl splitting at the Dirac point as shown in Fig. 4(e) because of protection offered by the zincblende point group symmetry. However, it is possible to reach the Weyl phase by straining to lower the crystalline symmetry or by using an external magnetic field to break time reversal symmetry [40].

IV. CONCLUDING REMARKS

In summary, the electronic structure of CdTe has been investigated by ARPES measurements and first-principles calculations. Our work not only provides critical spectroscopic information for CdTe, a compound of broad applications, but also demonstrates the topological distinction between CdTe and HgTe as well as the topological phase transition in the mixed compound $Hg_xCd_{1-x}Te$. Our results and methodology shed light onto experimental investigation on the 3D Dirac semimetal phase of $Hg_xCd_{1-x}Te$ at the critical composition and further experimental realization of long-sought Weyl fermions.

ACKNOWLEDGMENTS

This work was supported by Introducing Talents of Discipline to Universities No. B08040 and National Natural Science Foundation of China under Grant No. 51172185 (L.F.), the U.S. Department of Energy (DOE), Office of Science (OS), Office of Basic Energy Sciences, under Grant No. DE-FG02–07ER46383 (T.C.C.) and Grant No. DE-FG-02-05ER46200 (M.Z.H.). M.N. is partially supported by the US National Science Foundation Grant No. NSF-DMR-1006492. We thank M. Bissen and M. Severson for assistance with beamline operation at the Synchrotron Radiation Center, which was supported by the University of Wisconsin-Madison. T.M. and the beamline operations were partially supported by US National Science Foundation Grant No. NSF-DMR-1305583.

[1] G. A. Babonas, E. Z. Krivayte, and A. Yu. Shileyka, Sov. J. Opt. Technol. **37**, 401 (1970).
[2] C. Canali, F. Catellani, C. Jacoboni, R. Minder, G. Ottaviani, and A. Quaranta, Solid State Commun. **17**, 1443 (1975).
[3] D. Berlincourt, H. Jaffe, and L. R. Shiozawa, Phys. Rev. **129**, 1009(1963).
[4] J. Gu, T. Kitihara, S. Fujita, and T. Sakaguchi, Jpn. J. Appl. Phys. **14**, 499 (1975).
[5] A. L. Gentile, J. E. Kiefer, N. R. Kyle, and H. V. Winston, Mater. Res. Bull. **8**, 523 (1973).
[6] J. J. Loferski, J. Appl. Phys. **27**, 777 (1956).
[7] F. A. Selim and F. A. Kroger, J. Appl. Phys. **49**, 3737 (1978).
[8] C. S. Ferekides, D. Marinskiy, V. Viswanathan, B. Tetali, V. Palekis, P. Selvaraj, and D. L. Morel, Thin Solid Films **361-362**, 520 (2000).
[9] O. Limousing, C. Blondel, J. Cretolle, H. Dzitko, P. Laurent, F. Lebrum, J. P. Leray, M. Arques, N. Baffert, F. Mathy, A. Noca, P. Trystram, P. Villard, P. Baron, E. Delagnes, and M. Rouger, Nucl. Instrum. Methods A **442**, 244 (2000).
[10] T. Takahashi, and S. Watanabe, IEEE Trans. Nucl. Sci. **48**, 950 (2001).
[11] Y. Nemirovsky, A. Ruzin, G. Asa, and J. Gorelik, J. Electron Mater. **25**, 1221 (1996).
[12] K. Biswas, and M.-H. Du, New J. Phys. **14**, 063020 (2012).
[13] S. D. Barthelmy, Proc. SPIE **4140**, 50 (2000).
[14] S. Calnan and A. N. Tiwari, Thin Solid Films **518**, 1839 (2010).
[15] M. Z. Hasan and C. L. Kane, Rev. Mod. Phys. **82**, 3045 (2010).
[16] X.-L. Qi and S.-C. Zhang, Rev. Mod. Phys. **83**, 1057 (2011).
[17] B. A. Bernevig, T. L. Hughes, and S.-C. Zhang, Science **314**, 1757 (2006).
[18] M. König, S. Wiedmann, C. Brüne, A. Roth, H. Buhmann, L. W. Molenkamp, X.-L. Qi, and S.-C. Zhang, Science **318**, 766 (2007).
[19] M. Orlita, D. M. Basko, M. S. Zholudev, F. Teppe, W. Knap, V. I. Gavrilenko, N. N. Mikhailov, S. A. Dvoretskii, P. Neugebauer, C. Faugeras, A.-L. Barra, G. Martinez, and M. Potemski, Nat. Phys. **10**, 233 (2014).
[20] B.-J. Yang and N. Nagaosa, Nat. Commun. **5**, 4898 (2014).
[21] X. Wan, A. M. Turner, A. Vishwanath, and S. Y. Savrasov, Phys. Rev. B **83**, 205101 (2011).
[22] Z. Wang, Y. Sun, X.-Q. Chen, C. Franchini, G. Xu, H. Weng, X. Dai, and Z. Fang, Phys. Rev. B **85**, 195320 (2012).
[23] S. M. Young, S. Zaheer, J. C. Y. Teo, C. L. Kane, E. J. Mele, and A. M. Rappe, Phys. Rev. Lett. **108**, 140405 (2012).
[24] T. P. Humphreys, G. P Srivastava, and R. H. Williams, J. Phys. C: Solid State Phys. **19**, 1259 (1986).
[25] J. Chelikowsky, D. J. Chadi, and M. L. Cohen, Phys. Rev. B **8**, 2786 (1973).

[26] D. W. Niles and H. Höchst, Phys. Rev. B **43**, 1492 (1991).
[27] C. Janowttz, L. Kipp, R. Manzke, and B. A. Orlowski, J. Surf. Sci. **231**, 25 (1990).
[28] X. M. Zhang, R. S. Ma, X. C. Liu, G. Z. Xu, E. K. Liu, G. D. Liu, Z. Y. Liu, W. H. Wang, and G. H. Wu, Europhys. Lett. **103**, 57012 (2013).
[29] C. Hartwigsen, S. Goedecker, and J. Hutter, Phys. Rev. B **58**, 3641 (1998).
[30] X. Gonze, J.-M. Beuken, R. Caracas, F. Detraux, M. Fuchs, G.-M. Rignanese, L. Sindic, M. Verstraete, G. Zerah, F. Jollet, M. Torrent, A. Roy, M. Mikami, P. Ghosez, J.-Y. Raty, and D. C. Allan, Comput. Mater. Sci. **25**, 478 (2002).
[31] X. Gonze, G.-M. Rignanese, M. Verstraete, J.-M. Beuken, Y. Pouillon, R. Caracas, F. Jollet, M. Torrent, G. Zerah, M. Mikami, Ph. Ghosez, M. Veithen, J.-Y. Raty, V. Olevano, F. Bruneval, L. Reining, R. Godby, G. Onida, D. R. Hamann, and D. C. Allan, Zeit. Kristallogr. **220**, 558 (2005).
[32] G. Q. Li, W. Q. Jie, and T. Wang, Nucl. Instrum. Methods Phys. Res. Sect. A **534**, 511 (2004). The CdTe single crystals are supplied by Imdetek Ltd.
[33] C. Brüne, C. X. Liu, E. G. Novik, E. M. Hankiewicz, H. Buhmann, Y. L. Chen, X. L. Qi, Z. X. Shen, S. C. Zhang, and L. W. Molenkamp, Phys. Rev. Lett. **106**, 126803 (2011).
[34] C. Liu *et al.* (unpublished).
[35] S.-J. Tang, T. Miller, and T.-C. Chiang, Phys. Rev. Lett. **96**, 036802 (2006).
[36] L. S. Dang, G. Neu, and R. Romestain, Solid State Commun. **44**, 1187 (1982).
[37] T. Miller, W. E. McMahon, and T.-C. Chiang, Phys. Rev. Lett. **77**, 1167 (1996).
[38] G. Bian, X. Wang, T. Miller, and T.-C. Chiang, Europhys. Lett. **101**, 27004 (2013).
[39] G. B. Halasz and L. Balents, Phys. Rev. B **85**, 035103 (2012).
[40] D. Bulmash, C.-X. Liu, and X.-L. Qi, Phys. Rev. B **89**, 081106(R) (2014).